Proceedings of the 8th International Conference on MicroManufacturing
University of Victoria, Victoria, BC, Canada, March 25-28, 2013

An analytical model for calculating the temperature distribution and determining the laser forming mechanism

ICOMM
2013
99

Morgan A. Lok[1], Hideki Aoyama[2]
[1]Morgan A. Lok; System Design Engineering, Keio University, Japan; morgan.lok@gmail.com
[2]Hideki Aoyama; System Design Engineering, Keio University, Japan; haoyama@sd.keio.ac.jp

INTRODUCTION

Laser forming is a manufacturing method which uses laser induced thermal stress to plastically deform sheet metal. Due to the induced uneven thermal stresses and resulting bending moments, laser forming can deform sheet metal without the use of external forces. Laser forming can produce both simple line, and curved line bends, either of which can be spaced to form simple or complex surfaces. While slower than press or stamp forming, laser forming shows potential for use in small volume and prototype manufacturing since it does not require expensive dies or heavy machinery. Laser forming can also be used on brittle materials, and has negligible springback.

LASER FORMING MECHANISMS

There are three main laser forming mechanisms, with the determined resulting deformation shown in Table 1.

Table 1: Laser Forming Mechanisms

Mechanism	*Abbrev.*	*Deformation*	*Direction*
Thermal Gradient	TGM	Bending	Towards laser
Buckling	BM	Bending	Random
Upset	UM	Upsetting	Transverse

While a rough guideline provided by Arnet and Vollertsen [1] or FEM can be used to predict the mechanism, there are no quick analytical methods to accurately tell which mechanism would occur given specific input scanning parameters (laser diameter, power, scanning velocity, absorption, material thermo-mechanical properties, and material dimensions).

For the design of laser forming CAM systems, understanding how the mechanisms occur, which one will occur, and how much each parameter can be varied to stay within the TGM mechanism while controlling the bend angle, are essential for scanning path generation.

This research attempts to address these issues by developing an analytical model that can predict the mechanism that occurs when forming SUS304 stainless steel by stress-strain simulation of the material, and to give some insight into the laser forming mechanisms.

The analytical model makes use of a new method to calculate the temperature field analytically, by the use of Quasi-Monte Carlo integration. In order to simulate the stress-strain cycle in the material, an adaptation of a model used to predict thermal residual stresses [2] was utilized and combined with a model to predict laser forming deformation.

QUASI-MONTE CARLO TEMPERATURE CALCULATION

The analytical temperature simulation is modeled on Cheng & Lin's [3] adaptation of the Carslaw & Jaeger's [4] point heat source equation and the method of images. This method considers the past positions of the laser and the change in thermo-mechanical properties [5], and calculates the temperature as the superposition of change in temperature from all past and current laser locations. The Cheng & Lin model was originally used for a 1D sample of temperatures (mid-line temperatures), but in this research it was adapted to calculate the 3D temperature distribution.

$$T(x,y,z,t) = \frac{\eta q}{\rho c \pi^{1.5} \alpha^{0.5}} \int_{\tau=0}^{\tau=t} \frac{1}{\sqrt{t-\tau}[4\alpha(t-\tau)+\omega^2]} \times \exp\left[-\frac{(x-x')^2+(y-y')^2}{4\alpha(t-\tau)+\omega^2} - \frac{z^2}{4\alpha(t-\tau)}\right] d\tau \quad (1)$$

Where η is absorption, q is laser power in W, ρ is density in kg/m^3, α is thermal diffusivity in m/s^2, c is specific heat in J/K, ω is laser diameter in metres, and t is the current time in seconds.

Both x' and y' are used to define the position of the laser at a previous time, τ. As a result, they are both functions of τ, which is used to integrate up to the current time.

It was found that this temperature model was highly sensitive to the time (t,τ) and physical (x,y,z) resolutions used. A finer time resolution caused the temperature to approach infinity at the laser center, and had computational times roughly similar to FEM (over 20 hours), while a coarse x,y,z resolution resulted in highly inaccurate results. In addition, the number of required calculations increased exponentially as the time resolution increased, also known as the curse of dimensionality.

To address these problems and the high dimensionality, the integration was computed using Quasi-Monte Carlo (QMC).

First, samples are exponentially distributed for τ as follows:

$$f(\tau|\mu) = \begin{cases} 0 & \tau \geq t \\ t - \frac{1}{\mu} e^{\frac{-\tau}{\mu}} & t > \tau \geq 0 \\ 0 & \tau < 0 \end{cases} \quad (2)$$

where t is the current time, and $\mu = t/2$, which are both updated at every time step, along with all of the thermo-mechanical properties of the model. By using the negative exponential importance sampling of time, the majority of points are sampled near the current laser position in x, y, and t, where temperature changes are far more significant.

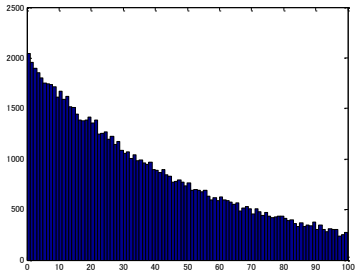

Fig. 1: Number of Samples vs. Time Steps away from Current Time t

Upon generating the τ values, these values are then used to generate corresponding quasi-random sampling points in x and y using a scrambled low-discrepancy 2-D Sobel sequence, which converges faster than pseudo-random sampling. The standard deviation of the Normal Distribution for sampling the points is as shown below.

$$\sigma_{QMC} = \sqrt{4\alpha_\tau(t-\tau)+\omega^2} \quad (3)$$

This standard deviation is different for every τ value, and changes with every time step increment, which affects the position in x and y of the sample.

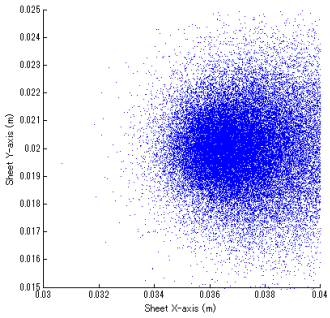

Fig. 2: Effect of Importance Sampling on Sampling Location

By using QMC, the time resolution issues were drastically mitigated, allowing for much coarser time steps with equivalent accuracy. Similarly, sensitivity to the physical resolution and size of the sheet was drastically reduced.

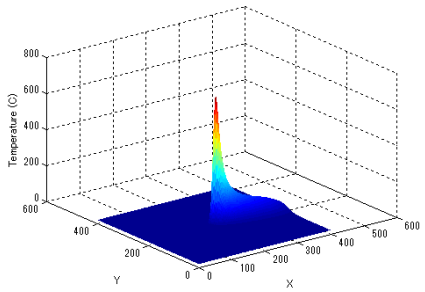

Fig. 3: A Generated Temperature Distribution

Overall the calculation time was shorted from 36 hours using FEM (ABAQUS), to 20 hours using the 3D Cheng & Lin method with a high resolution model. Using the QMC model, it takes 50 minutes to perform the equivalent analysis with a high time resolution of dt = 0.001s, or 5 minutes for a low resolution of dt = 0.01s for a 40x40x1mm piece. Either resolution produces accurate temperature results.

The results from the temperature simulation match well with Amada and Shirai's FEM simulation. It was found that the Method of Images worsens the prediction for thicknesses of 1mm and thicker, but when used on thicknesses of 0.1mm, it provides better results.

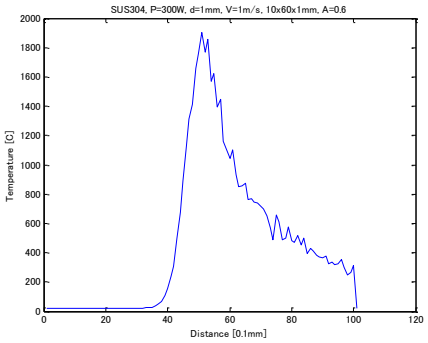

Fig. 4: Replicating Amada & Shirai's Simulation

LASER FORMING MECHANISM PREDICTION

To predict the Laser Forming Mechanism, a model was built to replicate the localized stress-strain cycle that occurs in the sheet due to both thermally induced strains and bending.

It was hypothesized that the laser forming mechanism can be predicted from the simulated stress-strain cycle and the plastic strain distribution. If plastic strain forms only at the top of the sheet, the mechanism is TGM [6], while if it forms at all depths but is uneven, the mechanism is BM.

A. MODELING THE LOCALIZED THERMAL STRAIN

Modeling of the thermally induced stress-strain cycle was based on the modeling of residual stresses formation in welding. During localized heating of the material, the surrounding cooler material is significantly stiffer and has a higher yield stress than the heated material, acting as if constraining the heated region and preventing local expansion. This translates the thermal expansion into compressive strain.

In this model, since the stress is always changing with temperature and plastic yielding, the calculations are written in terms of strain, which is more stable and easier to compute, especially in cases of unloading and reloading.

The material was modeled as springs in series, based on Murakawa's [2] modeling for residual stress prediction in welds. The stiffness of each spring is modeled as:

$$k_j = \frac{E_j(\sigma,T)a_j}{l_j} \quad (4)$$

where *E* is the Elastic or Plastic Modulus, *a* is the element cross-sectional area, and *l* is the element length.

In Murakawa's model, the heated element was modeled as one spring (k), and the non-heated elements as another (k*). The two are related via the variable β, which was stated as 1 in most situations.

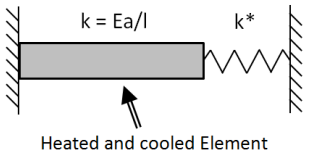

Fig. 5: Murakawa's Residual Stress Spring Model

$$\sigma = -\alpha E T_{max} \frac{k^*}{k+k^*} \quad (5)$$

$$\sigma = -\beta \alpha E T_{max} \quad (6)$$

Using $\beta = 1$ (fully constrained) by definition does not consider the flexing of the material, and is not appropriate for laser forming. Instead, all discretized elements in x,y, and z are modeled as individual spring in series in the transverse direction, and β was not used.

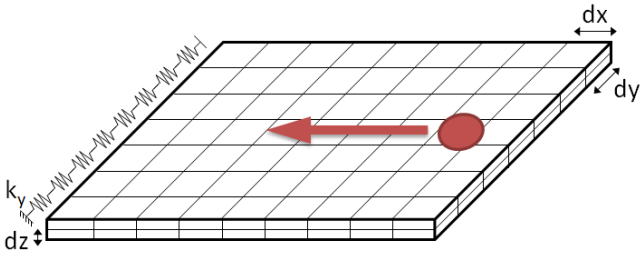

Fig. 6: Modeling of Material in Simulation

The mid-plane elongation Δl_{y0} in the y-direction is assumed to be constant for all x and z along the x-z face. Thus, treating all equivalent y-springs in x and z as springs in parallel, Δl_{y0} can be found.

$$\frac{1}{k_{y,eq(i,k)}} = \sum_{j=1}^{n} \frac{1}{k_{y(i,j,k)}} \quad (7)$$

$$\Delta l_{y(i,k)} = \sum_{j=1}^{n} \alpha_{th(i,j,k)} \Delta T_{(i,j,k)} dy \quad (8)$$

$$\Delta l_{y0} = \frac{\sum_{k=1}^{o} \sum_{i=1}^{m} k_{y,eq(i,k)} \Delta l_{y(i,k)}}{\sum_{k=1}^{o} \sum_{i=1}^{m} k_{y,eq(i,k)}} \quad (9)$$

The transverse force for each equivalent spring is found as follows.

$$F_{y(i,k)} = -k_{y,eq(i,k)} (\Delta l_{y(i,k)} - \Delta l_{y0}) \quad (10)$$

Using the transverse force, the equivalent displacement at each element can then be found using the local k values.

$$\Delta l_{y(i,j,k)} = \frac{F_{y(i,k)}}{k_{y(i,j,k)}} \quad (11)$$

The local thermal strain is then calculated for each element, with consideration of the thermal expansion:

$$\varepsilon_{th(i,j,k)} = \frac{\Delta l_{y(i,j,k)} - \alpha_{th(i,j,k)} \Delta T_{(i,j,k)} dy}{(\alpha_{th(i,j,k)} \Delta T_{(i,j,k)} + 1) dy} \quad (12)$$

B. MODELING THE STRESS-STRAIN CYCLE

Using the local thermal strain, the moment and curvature can be calculated. The curvature is then used to calculate the strain that occurs due to bending. This is done to simulate the material bending due to the imbalances of stresses, and relieving some strain during bending.

$$M = \sum E \varepsilon_{th} z dz \quad (13)$$

$$\frac{1}{\rho} = \frac{M}{\sum E z^2 dz} \quad (14)$$

$$\varepsilon_r = \frac{z}{\rho} \quad (15)$$

$$\varepsilon_t = \varepsilon_r + \varepsilon_{th} \quad (16)$$

The strain is then compared to the strain for the previous time step. The change in strain is then added to the elastic strain, and the yield strain is recalculated with respect to the new temperature.

$$\Delta \varepsilon = \varepsilon_t - \varepsilon_{t-1} \quad (17)$$

$$\varepsilon_{e,t} = \varepsilon_{e,t-1} + \Delta \varepsilon \quad (18)$$

If the localized strain is over the yield strain, the difference is is added to the plastic strain, and the elastic strain is set as the yield strain.

$$|\varepsilon_{e,t}| > |\varepsilon_{y,T}| \quad (19)$$

$$\varepsilon_{p,t} = \varepsilon_{p,t-1} + (\varepsilon_{e,t} - \varepsilon_{y,T}) \quad (20)$$

$$\varepsilon_{e,t} = \varepsilon_{y,T} \quad (21)$$

It is necessary to follow this approach, as the yield strain is changing at every time step due to the change in temperature.

Because of the changing yield strain and elastic and plastic moduli, the local stress decreases during plastic deformation and increasing temperature. The reverse is true during cooling. This leads to the stress and strain profiles of the shape shown in Figure 7.

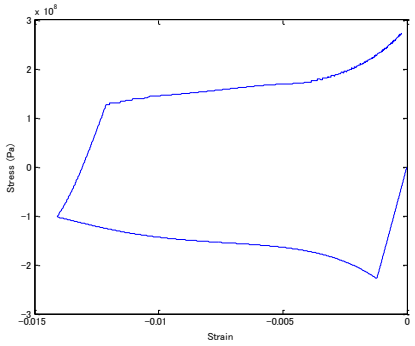

Fig. 7: Local Stress-Strain Cycle for Heated Material

While not shown in Figure 7, providing that the total developed plastic strain is small during heating ($\varepsilon > -0.005$), it is possible that the material returns to a stress that is lower than the yield stress during cooling.

VERIFICATION OF SIMULATION

C. EXPERIMENTAL VERIFICATION

Experimentation was undertaken to determine the TGM and BM bending parameters. An 808nm 30W diode laser was used, mounted on a 3-axis CNC gantry to scan the laser at constant speeds across the SUS304 samples. The laser is passed through a fiber optic cable, and through a collimating lens. The power was calibrated from the output that passed through the collimating lens.

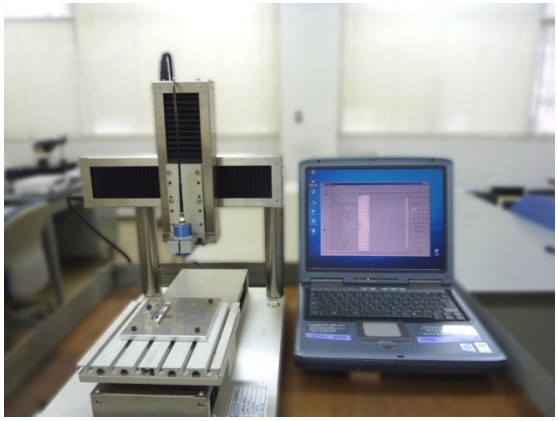

Fig. 8: Experiment Setup

In the testing, 150 samples of 10x30x0.1mm SUS304 steel were scanned near the focal point of the laser, varying only the power and velocity. The material was either uncoated, or coated with black ink to improve absorption. Downward bending is an indication of BM, while upward bending is either BM or TGM.

It was found that there is a marked relationship between the power and velocity, and the laser forming mechanism. There are distinct regions at which no bending will occur, TGM will occur, or BM will occur.

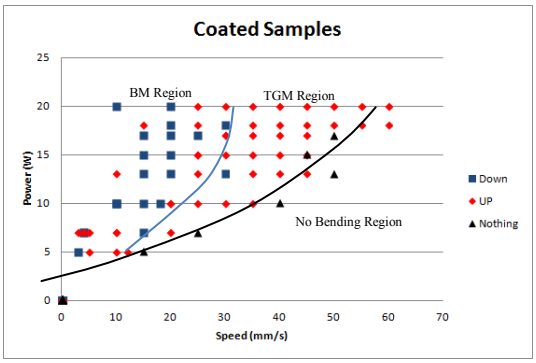

Fig. 9: Coated Sample Results

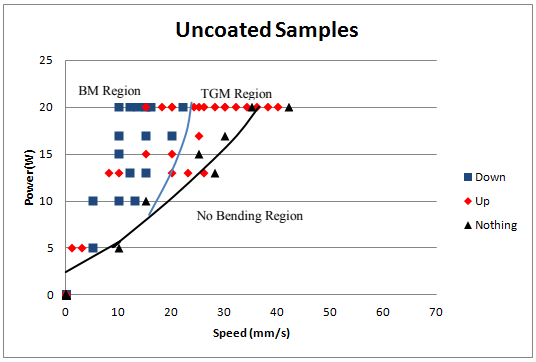

Fig. 10: Uncoated Sample Results

For BM, the radius of the bend and the bend angle are much larger than TGM. The material also appears to oxidize more on both the top and especially the bottom surfaces. This suggests that the temperature on the bottom surface of the material during TGM is much lower than for BM, in line with expectations.

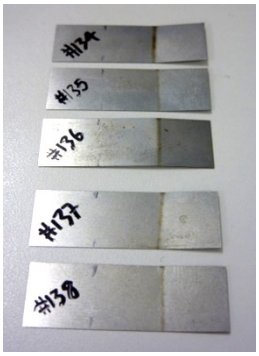

Fig. 11: Samples across the BM/TGM Border at 20W

In samples which had appeared not to bend, it was often obvious from inspection that some plastic deformation had occurred on the top surface. This suggests that as hypothesized, the bending does not cause plastic strain as in traditional press bending, but rather that the bending is caused by the localized stress-strain process.

D. SIMULATION OF EXPERIMENTAL PARAMETERS

Various parameters from the experimentation were attempted, and trends in the plastic and elastic strain histories were observed that correlate with the different mechanism regions as seen in the experimentation. The coated sample's absorption rate was estimated at 0.6, while the uncoated sample's absorption rate was estimated at 0.25 [7].

Within the TGM region parameters region for coated simulations (A=0.6), it was found that there were two types of results:

1. The bottom surface develops plastic strain
2. The bottom surface does not develop plastic strain

In other studies it has been found that TGM parameters do not produce plastic strain on the bottom surface, but instead when plastic strain is produced but forms consistent upward bending, it is called the Coupling Mechanism (CM) [6].

Thus, the mechanisms can be categorized by Table 2.

Table 2: Mechanism Categorization

Mechanism	*TGM*	*CM*	*BM*
Bottom Surface Plastic Strain Properties:	No plastic strain for all time	Positive plastic strain at start, then negative plastic strain	Negative plastic strain for all time

Parameters in the BM region produced no tensile plastic strain at the start of loading, and the final stress was often the yield stress at all layers. In contrast, for TGM and CM parameters there was a notable stress difference across layers when the thermal strain returned to zero strain after cooling.

E. COATED SAMPLE SIMULATION

In Figures 10-12, we can see for an 11 z-layer model (left-most dark blue line is the top layer, right-most teal is the bottom layer) the bottom layer's stress-strain cycle transitions from first generating positive plastic strain, to only generating negative plastic strain. This marks the transition from CM (Figures 10, 11) to BM (Figure 12).

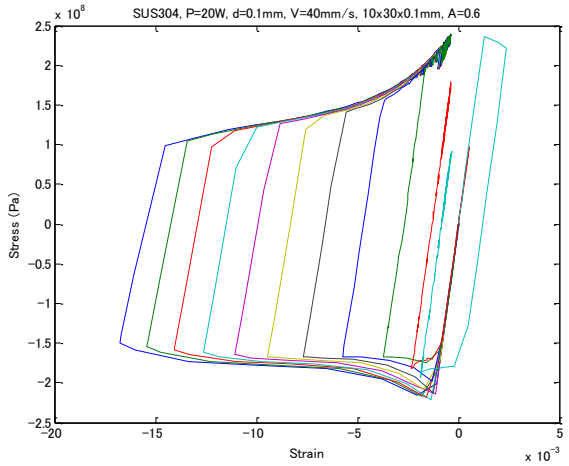

Fig. 12: Stress-Strain Cycle [CM, 20W, 40mm/s, Coated]

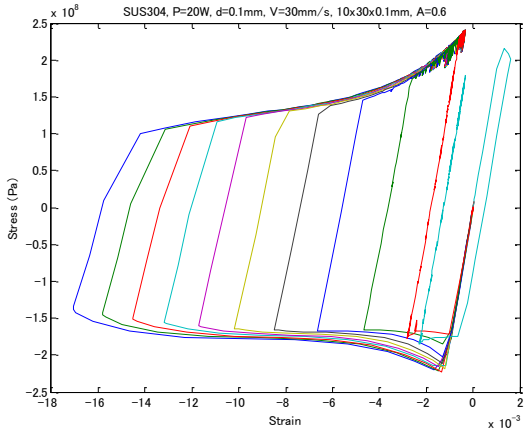

Fig. 13: Stress-Strain Cycle [CM, 20W, 30mm/s, Coated]

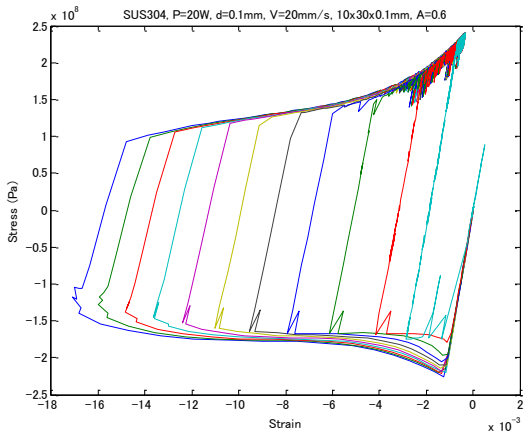

Fig. 14: Stress-Strain Cycle [BM, 20W, 20mm/s, Coated]

Comparing the various plastic strain histories versus the longitudinal distance, which can also be written as time due to constant velocity, a clearer difference can be seen in the plastic strain formation. Figures 13-15 show the laser forming process when the laser is 50% across the material. Notably the plastic strain on the bottom surface is positive at first for CM parameters. For BM parameters, the bottom surface plastic strain starts as negative, and remains negative for all time values.

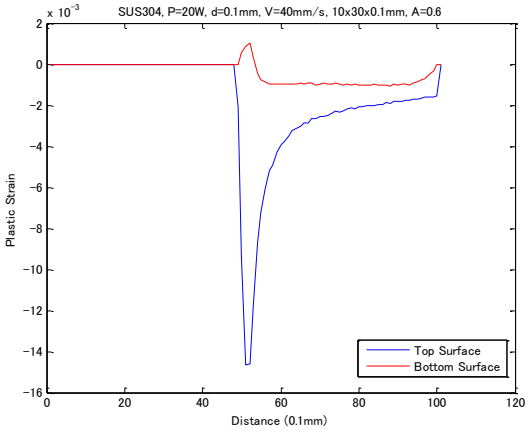

Fig. 15: Plastic Strain [CM, 20W, 40mm/s, Coated]

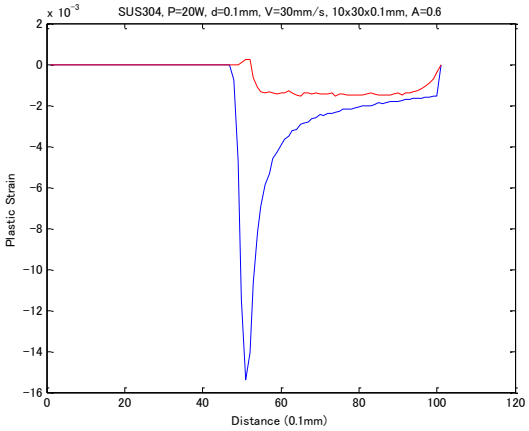

Fig. 16: Plastic Strain [CM, 20W, 30mm/s, Coated]

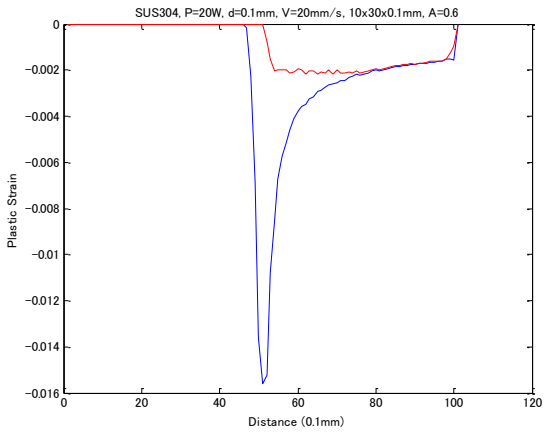

Fig. 17: Plastic Strain [BM, 20W, 20mm/s, Coated]

For lower laser powers, it was observed that no plastic strain is formed when simulating uncoated samples in the TGM region, due to the significantly lower absorption, and thus a lower bottom surface temperature. As a result there was no CM observed in the simulations.

F. UNCOATED SAMPLE SIMULATION

For uncoated sample simulations (A=0.25) the parameters in the TGM region produced no compressive plastic strain on the bottom material surface. However, the simulation still shows a clear difference between TGM and BM parameters.

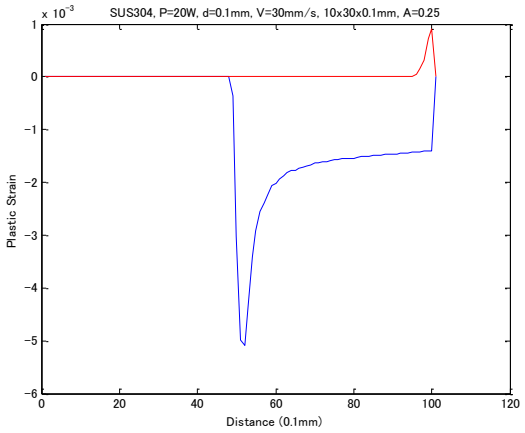

Fig. 18: Plastic Strain [TGM, 20W, 30mm/s, Uncoated]

G. SIMULATION RESULTS

When computing many different parameters from the experimentation, it was found that both the coated and uncoated sample simulations were accurate in predicting the border between the CM/BM, and TGM/BM mechanisms. However it was found that the results were not as accurate for uncoated sample simulation, especially at lower power settings. This may reflect the difference between the controlled absorption of the ink, and the highly varying absorption across uncoated samples, or the inappropriate choice of the absorption coefficient. The simulation results for multiple parameters are overlaid on top of the experimental results in Figures 19 and 20.

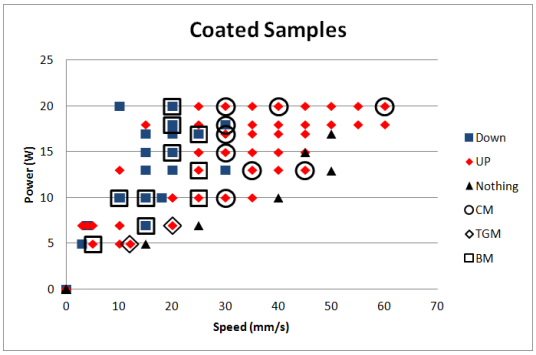

Fig. 19: Coated Experimental Results vs. Simulation Results

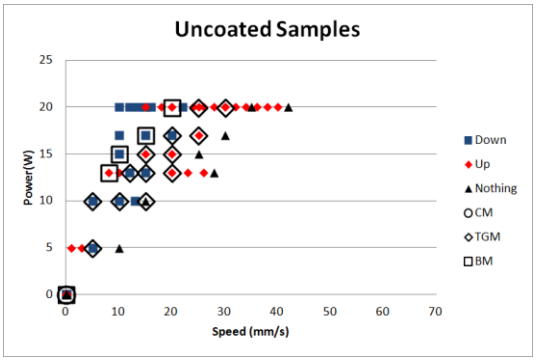

Fig. 20: Uncoated Experimental Results vs. Simulation Results

The simulation was also compared to other studies in the literature. When comparing the simulation data to Hsieh & Lin [8], the plastic transverse strain forms a similar shape. However, we do not see the initial positive plastic strain in their results as is present in this simulation. Using a velocity of 30mm/s as a substitute for time to replicate Hsieh & Lin's simulation parameters, the algorithm predicts TGM bending, with a maximum top surface temperature of 650˚C and bottom surface temperature of 250˚C. The difference in temperature to Hsieh & Lin's results may be due to the element being heated at the center of the laser for the entire 0.1s pulse in their simulation, while in this simulation the laser is scanned across the surface.

CONCLUSIONS

In this research, two new simulation methods were proposed. The first is a new method to calculate the 3D temperature distribution during point source heating such as laser forming, laser welding or welding, by utilizing Quasi-Monte Carlo integration. This significant improved the speed of calculation, from 36 hours in FEM to less than 1 hour in the proposed method, while significantly reducing time sampling and resolution issues. Results from this simulation were found to match well with other FEM calculation results.

The second simulation method proposed is a new method of calculating the local stress-strain history of the material to determine the bending mechanism. The mechanism regions were predicted using scanning parameters from experimentation. It was found that the bending mechanism can be accurately predicted for both coated and uncoated samples. For uncoated samples it was found that the accuracy was not as high as for coated samples, which could be due to highly varying absorption properties across samples or an inappropriate absorption coefficient. The simulation suggests that CM, TGM, and BM were present in the coated samples, but for uncoated samples only TGM and BM were present due to the lower bottom surface temperature.

The close match of simulation data to experimental data suggests that the laser forming mechanisms can be reasonably modeled as a residual thermal stress-strain problem, with a simple spring model, and can be quickly predicted using a combination of both of the proposed new methods and a high time resolution.

REFERENCES

[1] H. Arnet et al. "Extending Laser Bending for the Generation of Convex Shapes." *Proc. Inst. Mech. Eng. Part B J. Eng. Manuf.*, 1995; vol. 209, pp. 433–442.

[2] H. Murakawa, "Theoretical Prediction of Residual Stresses in Welded Structures," *Journal of the JWS*, 1996; vol. 65, no. 7, pp. 558–562.

[3] P.J. Cheng et al. "An Analytical Model for the Temperature Field in the Laser Forming of Sheet Metal." *J. Mater. Process. Technol.,* 2000; vol 101, no. 1–3, pp. 260–267.

[4] H.S. Carslaw, Conduction of Heat in Solids, Clarendon Press, London, 1959.

[5] Y. Sakumoto et al. "High-Temperature Properties of Stainless Steel for Building Structures,"*J. Struct. Eng.*, 1996; vol. 122, no. 4, pp. 399–406.

[6] Y. Shi et al. "Research on the mechanisms of laser forming for the metal plate," *Int. J. Mach. Tools Manuf.,* 2006; vol. 46, no. 12–13, pp. 1689–1697.

[7] Jao Hwa Kuang et al., "The Surface Absorption Coefficient of S304L Stainless Steel by Nd:YAG Micro-Pulse Laser", *Adv. Mat. Res.*, 2012, vols. 472-475, pp. 2531-2534.

[8] H.-S. Hsieh and J. Lin, "Thermal–mechanical analysis on the transient deformation during pulsed laser forming," *Int. J. Mach. Tools Manuf.*, 2004; vol. 44, no. 2–3, pp. 191–199.